

Molecular Rheology of Nanoconfined Polymer Melts

Ahmet Burak Yildirim,¹ Aykut Erbaş,^{2,3} and Luca Biancofiore^{1,2}

¹*Department of Mechanical Engineering, Bilkent University, 06800 Ankara, Turkey*

²*UNAM - National Nanotechnology Research Center and Institute of Materials Science & Nanotechnology, Bilkent University, 06800 Ankara, Turkey*

³*Institute of Physics, University of Silesia, Katowice, Poland*

(Dated: March 17, 2023)

We use non-equilibrium atomistic molecular dynamics simulations of unentangled melts of linear and star polymers ($C_{25}H_{52}$) to study the steady-state viscoelastic response under confinement within nanoscale hematite ($\alpha - Fe_2O_3$) channels. We report (i) the negative (positive) first (second) normal stress difference and (ii) the presence of viscoelastic tension at low shear rates. We link these effects to bond alignment such that chains near the surface can carry the elastic force exerted on the walls, which decays as the chains become more aligned in the flow direction as the shear rate increases.

Nanoscale confinement of polymeric liquids is often encountered at ultra-thin fluid film lubrication and nanomanufacturing [1, 2]. As the confinement of a solvent-free polymeric liquid (i.e., melt), h , approaches the dimensions of the constituting polymer chains (e.g., the radius of gyration R_G), effects that are otherwise not visible in bulk can influence the rheological properties of the liquid [3, 4]. For instance, as $h/R_G \rightarrow 1$, polymer chains can adjust their configuration to the confinement by forming well-defined and discrete molecular layers, and these layers can alter the shear response of the melt in comparison to bulk [5–9, 96]. Further, confining surfaces can directly interact and induce non-negligible forces as the surfaces approach each other [11, 12]. Additionally, the molecular variables, such as polymerization degree of chains, branching, and composition, can play roles in chain dynamics differently compared to bulk [13]. Thus, describing the rheological properties of polymer melts at nanoscale confinement requires alternative methods that can take care of phenomena arising from finite-system dimensions.

While continuum models rely on constitutive equations to establish a relationship between deformation and the stress tensor by introducing response functions (i.e., moduli) [14], they fall short of capturing the rheological response as one of the dimensions of the system becomes comparable to R_G [15–20]. Furthermore, a microscopic definition of the stress tensor can describe the viscoelastic response of melts if all the forces and coordinates of constituting atoms are available [3, 21], for instance, from molecular simulations. Nevertheless, such an approach can be computationally expensive as the system dimensions become larger or when longer sampling times are needed. Alternatively, leveraging the contributions of continuum and molecular models, the complex rheological response of polymer melts across different length scales can be captured [22–26].

In this work, we attempt to bridge molecular-scale phenomena and macroscopic behaviour of strongly-confined (i.e., nanoscale) polymeric melts under non-equilibrium conditions. By using extensive all-atom molecular dy-

namics (MD) simulations, we demonstrate that the microscopic stress tensor under steady-state shear deviates significantly from what the continuum model of a simple generalized Newtonian fluid (GNF) would predict. Our calculations show that these deviations lead to excess viscoelastic stress, which decreases as the confinement decreases ($h \gg R_G$) and eventually vanishes for bulk systems for a wide range of molecular conditions (e.g., chain topology and rigidity) and confinement levels. We further relate the excess stress with the spatial orientation of the carbon-carbon bonds of the chains near the surface. Unexpectedly, chains adsorbed on the surface lead to an effective polymer brush-like layer, further decreasing the shear response [27, 28].

All MD simulations were performed using LAMMPS MD package [29] (see the Supplemental Material for the simulation details). The interactions between the atoms are modelled by the standard 12/6 Lennard-Jones potential using DREIDING force field [88, 89]. Each simulation box contains at least $N = 128$ charge-neutral linear (pentacosane) or star (branched 3-arm, 9-octylheptadecane) $C_{25}H_{52}$ polymers equilibrated at $T = 372$ K at a pressure at $p = 1$ atm [90]. We control the chain rigidity through an angle potential penalizing chain bending [33, 34] as $U_{\text{angle}}(\theta) = k_{\theta}(\theta - \theta_0)^2$, where θ is the angle between triplets of atoms in a chain, $\theta_0 = 109.47^\circ$ is the equilibrium value of the angle [35, 89], and $k_{\theta} \equiv \epsilon = 50$ kcal/mol is the potential strength [88]. By varying k_{θ} , we obtain chains with varying relaxation dynamics [34, 36–38] and modify the contribution of the elastic forces without altering the molecular structure [33] for both polymer topologies.

The relaxation time of a polymer chain, λ , can be related to the timescale, in which its deformed state returns to its undeformed configuration. Thus, the competition between λ and the shear time scale can be used to define the deviations from equilibrium [27, 28], requiring us to estimate λ . For this reason, we refer to the time autocorrelation function (TACF) for the Rouse model, which

is valid for melt, and use the chain end-to-end vector \mathbf{r}_{ee}

$$\frac{\langle \mathbf{r}_{ee}(t) \cdot \mathbf{r}_{ee}(0) \rangle}{nb^2} = \sum_{p=1,3,\dots} \frac{8}{p^2\pi^2} \exp\left(-\frac{tp^2}{\tau_1}\right), \quad (1)$$

where n is the number of carbon atoms in a chain, b^2 is the mean-square distance between adjacent beads (hence nb^2 is the equilibrium mean-square end-to-end distance of chains), τ_p is the spectrum of the relaxation times for the corresponding mode p . A visual definition of \mathbf{r}_{ee} is given in the inset of Fig. 1(a). The relaxation dynamics are dominated by the slowest mode ($p = 1$) [36, 39], allowing us to use $\lambda \approx \tau_1$. Note that the definition of \mathbf{r}_{ee} is not straightforward for branched polymers owing to the presence of more than two free ends [40]; thus, we modify the \mathbf{r}_{ee} definition for star polymers by considering the branching point to the corner vectors and track the mean-square end-to-end vectors over time (Fig. 1(b), inset).

To obtain λ for linear and star polymers from our simulations, we calculate the equilibrium (i.e., no shear) TACF for three chain rigidities by using our trajectories: $k_\theta = 0.1\epsilon$, $k_\theta = \epsilon$ and $k_\theta = 10\epsilon$ by fitting the correlation function to $\langle \mathbf{r}_{ee}(t) \cdot \mathbf{r}_{ee}(0) \rangle / \langle \mathbf{r}_{ee}(0) \cdot \mathbf{r}_{ee}(0) \rangle \propto \exp(-t/\lambda)$ (Fig. 1). We obtain the Rouse times as $\lambda_{\text{linear}}^{(0.1\epsilon)} = 7.07$ ns, $\lambda_{\text{linear}}^{(1\epsilon)} = 20.8$ ns, $\lambda_{\text{linear}}^{(10\epsilon)} = 29.14$ ns, for linear polymers; $\lambda_{\text{star}}^{(0.1\epsilon)} = 5.73$ ns, $\lambda_{\text{star}}^{(1\epsilon)} = 9.10$ ns, $\lambda_{\text{star}}^{(10\epsilon)} = 13.53$ ns, for star polymers. As the chain flexibility increases (i.e., $k_\theta \rightarrow 0$), the chain needs less time to recover, asymptotically leading to $\lambda \rightarrow 0$ in the case of monomers [22]. This relation between λ and chain rigidity (i.e., $\lambda^{(10\epsilon)} > \lambda^{(1\epsilon)} > \lambda^{(0.1\epsilon)}$) is quantita-

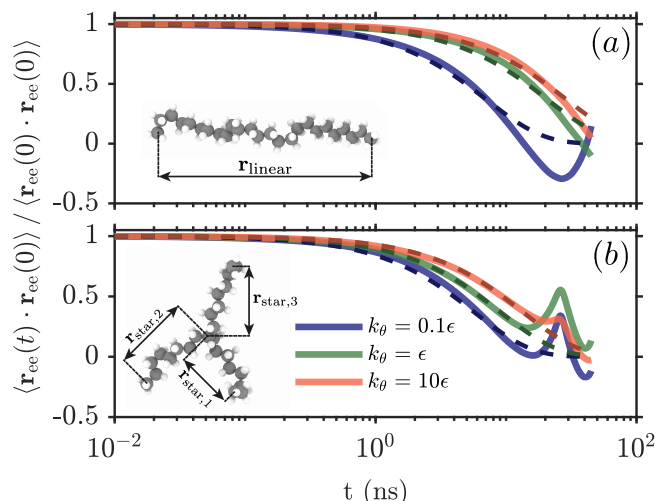


FIG. 1: Calculation of the relaxation times of the linear and star polymers for varying chain stiffness. Normalized time-autocorrelation function vs. time for (a) linear and (b) star polymers. The dashed lines denote the exponential fit associated with TACF.

tively consistent with the previous results [36, 41], and so does the relation between λ and the polymer topology (i.e., $\lambda_{\text{linear}} > \lambda_{\text{star}}$) [42]. Moreover, stiffening the chains increases the Kuhn size, which results in varying the chain rigidity to scale with the Kuhn sizes [15, 33, 43].

Next, we compare the steady-state rheology of the confined polymer melts to their bulk state under planar Couette flow to explore the confinement effects. We run shear simulations of (i) the bulk melts by deforming the simulation box (Fig. 2(a), inset) and (ii) the confined melts by moving the top and bottom surfaces (i.e., fixed and rigid hematite, $\alpha\text{-Fe}_2\text{O}_3$, layers) at constant velocity in the $\pm x$ -directions (Fig. 2(b), inset). We set the confinement level to $h = 5.57$ nm (for $N = 216$) to ensure that the pressure over the walls is the same as the hydrostatic pressure in bulk (i.e., $p = 1$ atm). Thus, any change in the (microscopic) stress tensor purely represents the flow characteristics.

From the simulation trajectories, the microscopic stress tensor $\boldsymbol{\sigma}$ can be calculated using the virial theorem [3, 44, 45]. Consequently, the ensemble-averaged total

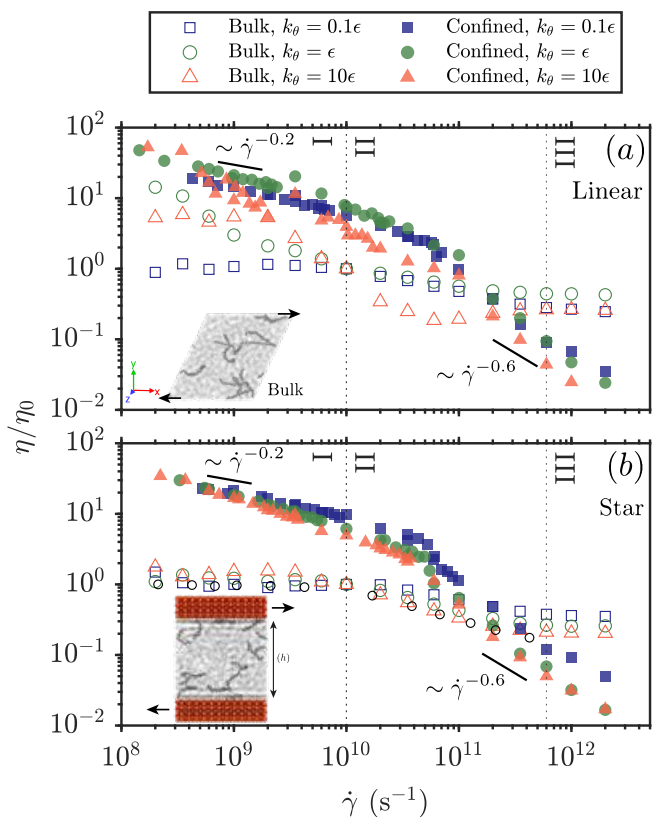


FIG. 2: Viscosity normalized with respect to the Newtonian plateau for the bulk (empty markers) and the confined (filled markers) configurations for the linear (a) and the star polymers (b). The black circles denote the viscosity values obtained by McCabe et al. [90] for unaltered star polymer ($k_\theta = \epsilon$). Error bars are of the size of markers.

stress tensor, composed of the kinetic and virial contributions, is prone to thermal fluctuations [46]. Therefore, we compute the total stress tensor of the melt in bulk and confined configurations and consider the time-averaged steady-state stress to eliminate thermal fluctuations. We define the macroscopic equivalent formulation [47]

$$\boldsymbol{\sigma} \equiv \underbrace{-p\mathbf{I} + 2\eta(\dot{\boldsymbol{\gamma}})\dot{\boldsymbol{\gamma}}}_{\text{GNF}} + \boldsymbol{\sigma}^{(\text{VE})}, \quad (2)$$

where p is the mechanical pressure of the melt, $p = -\frac{1}{3}(\sigma_{xx} + \sigma_{yy} + \sigma_{zz})$, $\dot{\boldsymbol{\gamma}}$ is the strain rate tensor with the only nonzero components, namely the shear rate, $\dot{\boldsymbol{\gamma}} = \dot{\gamma}_{xy} = \dot{\gamma}_{yx}$, and the extra-stress component for the viscoelastic effects $\boldsymbol{\sigma}^{(\text{VE})}$. As $\boldsymbol{\sigma}^{(\text{VE})} \rightarrow 0$, Eq. 2 reduces to the GNF stress tensor, which introduces the shear-dependency to the Newtonian viscosity η_0 [47–50].

To characterize the shear-dependent viscosity of our melts, we calculate the normalized viscosity, η/η_0 , where the shear viscosity is defined as $\eta \equiv \sigma_{xy}/\dot{\gamma}$, and the Newtonian viscosity is η_0 [51]. The observed behaviour of viscosity for bulk and confinement shows the expected shear-thinning behaviour (for linear: Fig. 2(a), for star: Fig. 2(b)) [90]. In Fig. 2, three regions are labelled to indicate the various shear responses; I, II, and III indicate the 1st Newtonian plateau, the shear-thinning regime, and the 2nd Newtonian plateau for bulk polymers, respectively.

The linear polymers in bulk tend to form crystalline structures at the Newtonian plateau for $k_\theta = \epsilon$ and $k_\theta = 10\epsilon$ cases. This leads to a higher viscosity than the zero-shear viscosity [20, 52], independent of the size of our simulation boxes (see Supplemental Material, Fig. S1). The flow-induced crystallization starts to vanish as the shear rate increases [53–55]. Notably, we do not observe crystallization for strongly flexible chains (i.e., $k_\theta = 0.1\epsilon$), which is a common simulation scheme for coarse-grained models [56, 57]. In the confined geometry, the viscosity of both polymer topologies is higher than their bulk states and monotonically decreases with the shear rate (Fig. 2) [44]. This decrease follows the power law $\eta \sim \dot{\gamma}^{-0.2}$ until shear bands start to develop in region II. In the transition regime, the Couette velocity profile starts to become centrally localized in the middle of the channel, disrupting the smoothness of the velocity profile [58–60]. With increasing shear rate, a discontinuity in the velocity profile develops, resulting in plug slip behaviour, and the decrease in viscosity follows the power law $\eta \sim \dot{\gamma}^{-0.6}$ (see Supplemental Material, Figs. S2 and S3 for velocity profiles). As the flexibility of the chains increases, the shear-thinning behaviour becomes stronger. Notably, if we replace our chains with monomers (i.e., no chains) and run separate simulations, no additional resistance due to the confinement appears (see Supplemental Material, Fig. S4), highlighting the role of chain connectivity.

To quantify the viscoelastic contributions to the total rheological response, we turn our attention back to the stress tensor $\boldsymbol{\sigma}$ (Eq. 2) and focus on the viscoelastic part of the stress tensor, $\boldsymbol{\sigma}^{(\text{VE})}$. According to Larson [61], viscoelasticity originates from unequal normal stress components, characterized by normal stress differences, with notable exceptions of the suspensions of non-Brownian non-spherical particles and porous polymer gels [62–65]. Hence, the viscoelastic stress is a function of the normal stress differences, $\boldsymbol{\sigma}^{(\text{VE})}(N_1, N_2)$ [47]. For concentrated polymeric liquids, the first and second normal stress differences ($N_1 = \sigma_{xx} - \sigma_{yy}$ and $N_2 = \sigma_{yy} - \sigma_{zz}$) arise due to the interactions between the chains trapped near the surfaces and the micro-structure dynamics, respectively [66]. Normal-stress differences govern the viscoelasticity in the scope of polymer melts, meaning that shear-thinning fluids are not necessarily viscoelastic as well [61, 62].

In Fig. 3, we explore the normal stress differences and the viscoelastic stress component as a function of the Weissenberg number ($Wi = \dot{\gamma}\lambda$) and the film thickness h . The Weissenberg number essentially characterizes the degree of non-linearity in the deformation behaviour of viscoelastic materials. When $Wi \ll 1$, the fluid exhibits characteristics similar to a Newtonian fluid. However, the fluid displays viscoelastic effects for $Wi \geq O(1)$ as normal forces become more dominant than shear forces, causing the polymers to stretch and store elastic energy [24]. Noting that $N_1 = N_2 = \sigma_{yy}^{(\text{VE})} = 0$ for $Wi = 0$, we observe an unexpected behavior for the normal stress differences; $N_1 < 0$ and $N_2 > 0$ leading to viscoelastic tension for $Wi < 50$. Within the practical limits of our MD simulations, we determine that $\sigma_{yy}^{(\text{VE})}$ increases up to $Wi \approx 3$ and decreases afterward (Fig. 3(a-f), shown with arrows). Approximately after $Wi = 100$, both the normal stress differences change sign, $N_1 > 0$ and $N_2 < 0$, also yielding $\sigma_{yy}^{(\text{VE})} < 0$ (i.e., viscoelastic compression). When confined within the same Wi interval, the same behaviour is present for both linear and star polymer topologies. On the other hand, for bulk systems, we observe $N_1 = N_2 = \sigma_{yy}^{(\text{VE})} \approx 0$, suggesting that the storage of the elastic energy depends on the restriction of movement of chains once confined.

To explore the change in N_1 and N_2 as a function of h , we change the film thickness while keeping the density constant (i.e., for each thickness h , N/h is preserved by varying N). In this way, we show how the normal stress differences increase in magnitude as the film thickness decreases (Fig. 3(g)). As h increases, ideally approaching the bulk system, the normal stress differences decrease substantially in magnitude and even change sign while retaining the same ratio N_1/N_2 , resulting in the well-known behavior of polymeric liquids with $N_2 < 0$ [19, 22, 42, 61, 62, 67, 68]. As achieving smaller film thickness becomes experimentally harder to achieve, this hints at why negative N_1 , positive N_2 , and hence vis-

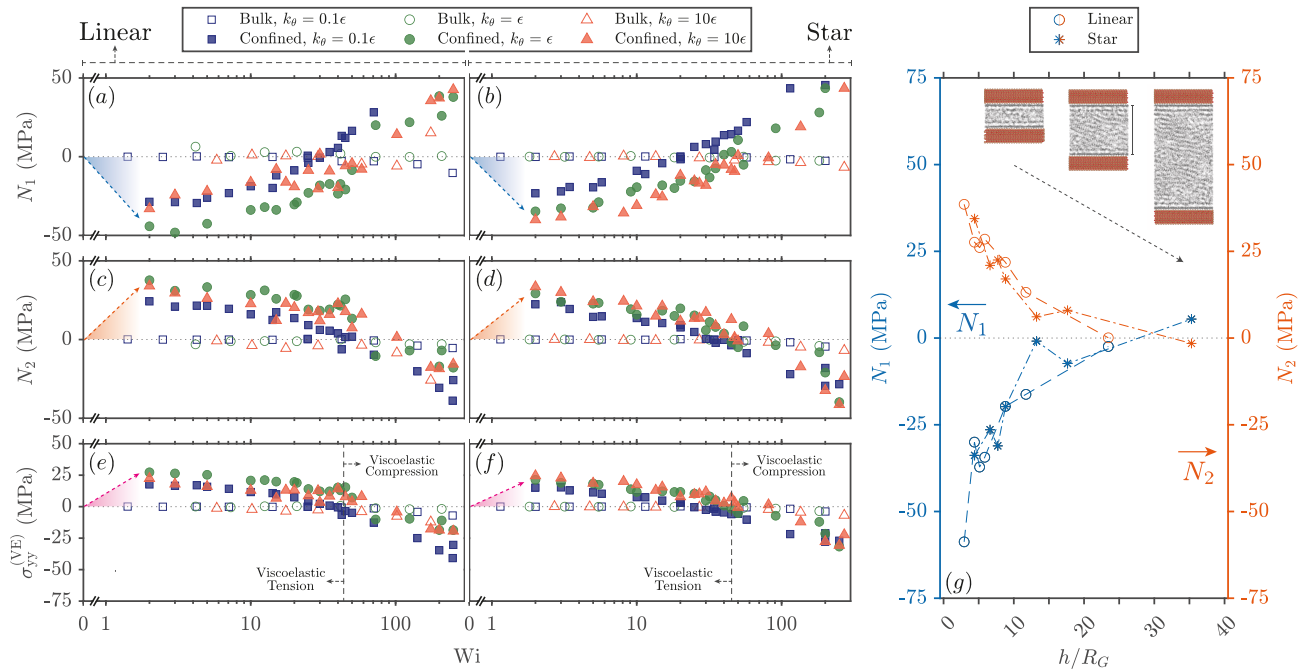


FIG. 3: Normal stress differences N_1 , N_2 and viscoelastic stress component opposing the streamwise direction $\sigma_{yy}^{(VE)}$. N_1 for linear (a) and star (b) polymers). N_2 for linear (c) and star (d) polymers. $\sigma_{yy}^{(VE)}$ for linear (e) and star (f) polymers, highlighting the regions of viscoelastic tension and compression applied to the walls. (g) N_1 and N_2 for the ratio of film thickness h to the radius of gyration R_G at $Wi = 10$ (see Supplemental Material, Fig. S5 for R_G). Note that the horizontal axes (a-d) are interrupted. Error bars are of the size of markers.

coelastic tension are not usually observed via experiments while having large magnitudes [19, 69]. As the normal stress differences, and hence the viscoelastic stress component, become smaller for larger h , constitutive models, such as GNF, show less deviation from the real microscopic behavior (Figs. 3(a-f)).

We relate the unexpected behavior of the normal stress differences to the alignment of the bonds constituting the chains since we do not observe significant changes in the chain end-to-end distance (see Supplemental Material, Fig. S6 for $R_{G,x}$ and $R_{G,y}$ behavior near - and away from - the surfaces) [70–73, 96]. For this purpose, we calculate the bond-orientation tensor, where we represent each bond independently, with the following formulation [74, 75]

$$Q_{\alpha\beta} = \frac{1}{N} \sum_N \frac{1}{N_b - 1} \sum_{j=1}^{N_b-1} \frac{b_{j\alpha} b_{j\beta}}{\|b\|^2}, \quad (3)$$

where N is the number of chains, N_b is the number of carbon atoms in a polymer chain, b_j for $1 \leq j \leq N_b - 1$ is the bond vector between consecutive carbon atoms in the same chain, and $\|b\|$ is the Euclidean length of the bond. To capture the near-surface dynamics, we refer to the yy -component of the bond-orientation tensor (i.e., Q_{yy}), representing the alignment of bonds against the flow.

To characterize the spatial variation in Q_{yy} , we con-

sider $Q_{yy} = \int_0^h q_{yy}(y) dy$ with the discretization $Q_{yy} \approx \sum_0^h q_{yy}(y) \Delta y$, where $\Delta y \approx 0.5\text{\AA}$. With this, we exploit the *local* bond orientation q_{yy} among confined channels in Fig. 4, where the representative snapshots color-codes the bond orientation such that the bond aligned vertically to the flow are red and those horizontal are given in blue. A visual inspection reveals a strongly adsorbed polymer layer between the surface and the bulk chains. This *viscoelastic* layer rather resembles a polymer brush with surface-grafted chains [27]. Notably, throughout our simulations, adsorbed chains do not exchange with the bulk chains (see the movie S7 in the Supplemental Material). When the surfaces are separated from each other, although the near-surface peak of q_{yy} is preserved, the bonds, overall, become more aligned with the flow in the x -direction throughout the channel, leading to a decrease in q_{yy} (Fig. 4(c)). At relatively fast shear rates (e.g., $Wi > 50$), the bonds become more aligned in the flow direction, leading to a decrease in q_{yy} . At lower shear rates (e.g., $Wi < 50$), the chains have more time to reorient to their entropically favoured states, creating additional viscoelastic force acting on the surfaces (Fig. 4(d)) [76–78]. Consequently, at lower Wi , the load-carrying capacity of the melt increases drastically, resulting in stresses orders of magnitude larger than in bulk ($\sigma_{yy}^{(VE)} \sim 25$ MPa vs. $p \sim 0.1$ MPa, see Fig. 3(e,f)). Importantly, the thickness of the polymer-adsorbed layer is independent of h ,

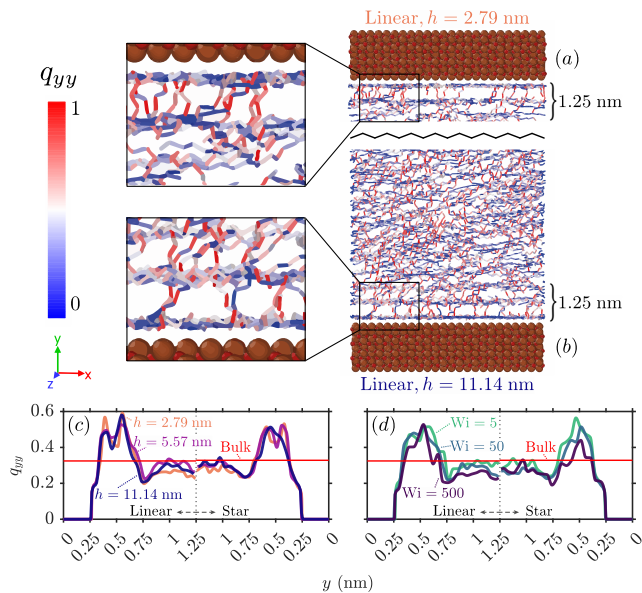


FIG. 4: Local bond orientation, q_{yy} . Snapshots of the spatial resolution of q_{yy} , for $h = 2.79$ nm (a) and $h = 11.14$ nm at $Wi = 10$ for linear polymers. Spatial variation of q_{yy} for different h for linear (left) and star polymers (right) (c) and for varying Wi for linear (left) and star polymers (right) (d).

and thus, the contribution of this layer to the overall viscoelastic response decreases as $h/R_G \rightarrow \infty$.

Our results demonstrate unexpected, sign-reversed normal stresses, namely N_1 and N_2 , together with the emergence of a viscoelastic tension and compression as the confinement dimension approaches that of the confined molecules. We observe a peculiar orientation of the near-surface chains. Our simulations suggest that the chains near the surface can be responsible for the elastic force exerted on the surface walls, and this effect can decay as the chains become more aligned with the flow at higher shear rates (i.e., $Wi \gg 1$). Excess tension emerges within a viscoelastic boundary layer, in which chains are vertically aligned, resulting in an increase in the load-carrying capacity of the confined melt. We observe smaller (larger) stresses for more flexible (rigid) chains for the two chain topologies we consider here, namely linear and star polymers. Notably, the stress components show weak sensitivity to the persistence length. We further reveal the dependence of the relaxation time on the chain rigidity, such that, by varying the chain rigidity, we modify the contribution of the elastic forces without altering the molecular structure [33]. Our study is limited to the polymer melts of linear and star polymers confined with rigid iron-oxide walls. Introducing the flexibility of the walls should reduce the observed effect, and slip and adsorption may depend on the polymer surface type [79–85]. Furthermore, it is yet to be explored whether this effect is typical for polymer melts, observable in more complex

polymer liquids under higher pressures or different surface roughness conditions [38, 86, 87].

The authors would like to acknowledge the The Scientific and Technological Research Council of Turkey (TUBITAK) for supporting this work under the project 221M576. The numerical calculations reported in this paper were partially performed at the TÜBİTAK ULAK-BİM, High Performance and Grid Computing Center (TRUBA resources).

- [1] I. Nezbeda and J. Škvára, *Molecular Simulation* **47**, 846 (2021).
- [2] B. Bhushan, *Springer Handbook of Nanotechnology* (Springer, 2017).
- [3] B. D. Todd and P. J. Daivis, *Nonequilibrium molecular dynamics: Theory, algorithms and applications* (Cambridge University Press, 2017).
- [4] D. Savio, N. Fillot, P. Vergne, H. Hetzler, W. Seemann, and G. E. Morales Espejel, *Journal of Tribology* **137**, 031502 (2015).
- [5] X. Zheng, H. Zhu, B. Kosasih, and A. Kiet Tieu, *Wear* **301**, 62 (2013).
- [6] C. Drummond and J. Israelachvili, *Macromolecules* **33**, 4910 (2000).
- [7] C. M. Mate, *Tribology on the small scale a bottom up approach to friction, lubrication, and wear* (Oxford University Press, 2008).
- [8] S. Yamada, *Tribology Letters* **13**, 167 (2002).
- [9] A. M. Smith, J. E. Hallett, and S. Perkin, *Proceedings of the National Academy of Sciences* **116**, 25418 (2019).
- [10] J. N. Israelachvili, *Intermolecular and surface forces* (Academic Press is an imprint of Elsevier, 2012).
- [11] B. Derjaguin and N. Churaev, *Journal of Colloid and Interface Science* **49**, 249 (1974).
- [12] E. Lifshitz and M. Hamermesh, The theory of molecular attractive forces between solids, in *Perspectives in Theoretical Physics*, pp. 329–349, Elsevier, 1992.
- [13] A. Karatrantos, R. J. Composto, K. I. Winey, M. Kröger, and N. Clarke, *Polymers* **11**, 876 (2019).
- [14] A. Morozov and S. E. Spagnolie, Introduction to complex fluids, in *Complex Fluids in Biological Systems*, pp. 3–52, Springer New York, 2014.
- [15] B. J. Kirby, *Micro- and Nanoscale Fluid Mechanics* (Cambridge University Press, 2012).
- [16] H. Ahmed and L. Biancofiore, *Journal of Non-Newtonian Fluid Mechanics* **292**, 104524 (2021).
- [17] S. Gamaniel, D. Dini, and L. Biancofiore, *Tribology International* **160**, 107011 (2021).
- [18] M. Paggi and D. Hills, editors, *Modeling and Simulation of Tribological Problems in Technology* (Springer International Publishing, 2020).
- [19] M. T. Shaw, *Introduction to Polymer Rheology* (John Wiley & Sons, Inc., 2011).
- [20] M. H. Nafar Sefiddashti, B. J. Edwards, and B. Khomami, *Physical Review Research* **2**, 013035 (2020).
- [21] M. Doi and S. F. Edwards, *The theory of Polymer Dynamics* (Clarendon Press, 1986).
- [22] J. Rudisill and P. Cummings, *Fluid Phase Equilibria* **88**,

- 99 (1993).
- [23] D. M. Holland, M. K. Borg, D. A. Lockerby, and J. M. Reese, *Computers & Fluids* **115**, 46 (2015).
- [24] A. N. Morozov and W. van Saarloos, *Physics Reports* **447**, 112 (2007).
- [25] P. J. Carreau, *Transactions of the Society of Rheology* **16**, 99 (1972).
- [26] M. Laso and H. Öttinger, *Journal of Non-Newtonian Fluid Mechanics* **47**, 1 (1993).
- [27] A. Erbaş and J. Paturej, *Soft Matter* **11**, 3139 (2015).
- [28] A. N. Semenov, *Langmuir* **11**, 3560 (1995).
- [29] A. P. Thompson *et al.*, *Computer Physics Communications* **271**, 108171 (2022).
- [30] S. L. Mayo, B. D. Olafson, and W. A. Goddard, *The Journal of Physical Chemistry* **94**, 8897 (1990).
- [31] S. K. Das, M. M. Sharma, and R. S. Schechter, *The Journal of Physical Chemistry* **100**, 7122 (1996).
- [32] C. McCabe, S. Cui, P. T. Cummings, P. A. Gordon, and R. B. Saeger, *The Journal of Chemical Physics* **114**, 1887 (2001).
- [33] R. Everaers, S. K. Sukumaran, G. S. Grest, C. Svaneborg, A. Sivasubramanian, and K. Kremer, **303**, 5 (2004).
- [34] R. Auhl, R. Everaers, G. S. Grest, K. Kremer, and S. J. Plimpton, *The Journal of Chemical Physics* **119**, 12718 (2003).
- [35] W. D. Callister and D. G. Rethwisch, *Materials science and engineering: An introduction* (John Wiley and Sons Australia, Ltd, 2021).
- [36] J. T. Kalathi, S. K. Kumar, M. Rubinstein, and G. S. Grest, *Macromolecules* **47**, 6925 (2014).
- [37] M. Ripoll, R. G. Winkler, and G. Gompper, *Physical Review Letters* **96**, 188302 (2006).
- [38] J. D. Halverson, G. S. Grest, A. Y. Grosberg, and K. Kremer, *Physical Review Letters* **108** (2012).
- [39] M. Doxastakis, D. N. Theodorou, G. Fytas, F. Kremer, R. Faller, F. Müller-Plathe, and N. Hadjichristidis, *The Journal of Chemical Physics* **119**, 6883 (2003).
- [40] Y.-F. Hu, K.-L. Xue, X.-C. Yu, and J.-X. Hou, *Journal of Polymer Research* **26**, 192 (2019).
- [41] L. A. Moreira, G. Zhang, F. Müller, T. Stuehn, and K. Kremer, *Macromolecular Theory and Simulations* **24**, 419 (2015).
- [42] A. Jabbarzadeh, J. Atkinson, and R. Tanner, *Tribology International* **35**, 35 (2002).
- [43] Y. Ding and A. P. Sokolov, *Journal of Polymer Science Part B: Polymer Physics* **42**, 3505 (2004).
- [44] S. Itoh, Y. Ohta, K. Fukuzawa, and H. Zhang, *Tribology International* **120**, 210 (2018).
- [45] J. Z. Yang and S. Du, *Calculation of cauchy stress tensor in molecular dynamics system with a generalized irving-kirkwood formulism*, 2014.
- [46] J. Z. Yang, X. Wu, and X. Li, *The Journal of Chemical Physics* **137**, 134104 (2012).
- [47] R. I. Tanner, *Engineering rheology* (Oxford Univ. Press, 2002).
- [48] H.-C. Tseng, *Journal of Rheology* **64**, 493 (2020).
- [49] M. O. Deville and T. B. Gatski, *Mathematical Modeling for Complex Fluids and Flows* (Springer Berlin Heidelberg, Berlin, Heidelberg, 2012).
- [50] H. Ahmed and L. Biancofiore, *Physics of Fluids* **34**, 103103 (2022).
- [51] S. Bair, C. McCabe, and P. T. Cummings, *Physical Review Letters* **88**, 058302 (2002).
- [52] G. Qu, J. J. Kwok, and Y. Diao, *Accounts of Chemical Research* **49**, 2756 (2016).
- [53] M. Boutaous, P. Bourgin, and M. Zinet, *Journal of Non-Newtonian Fluid Mechanics* **165**, 227 (2010).
- [54] R. S. Graham, *Journal of Engineering Mathematics* **71**, 237 (2011).
- [55] A. Jabbarzadeh and R. I. Tanner, *Macromolecules* **43**, 8136 (2010).
- [56] G. S. Grest, *MRS Proceedings* **464**, 71 (1996).
- [57] R. Everaers, S. K. Sukumaran, G. S. Grest, C. Svaneborg, A. Sivasubramanian, and K. Kremer, *Science* **303**, 823 (2004).
- [58] J. P. Ewen, H. A. Spikes, and D. Dini, *Tribology Letters* **69**, 24 (2021).
- [59] J. P. Ewen, C. Gattinoni, J. Zhang, D. M. Heyes, H. A. Spikes, and D. Dini, *Physical Chemistry Chemical Physics* **19**, 17883 (2017).
- [60] T. Nimura and T. Tsukahara, *Fluids* **7**, 241 (2022).
- [61] R. G. Larson, *Constitutive equations for polymer melts and solutions* (Butterworths, 2019).
- [62] O. Maklad and R. Poole, *Journal of Non-Newtonian Fluid Mechanics* **292**, 104522 (2021).
- [63] C. O. Osuji and D. A. Weitz, *Soft Matter* **4**, 1388 (2008).
- [64] A. Montesi, A. A. Peña, and M. Pasquali, *Physical Review Letters* **92**, 058303 (2004).
- [65] H. C. de Cagny, B. E. Vos, M. Vahabi, N. A. Kurniawan, M. Doi, G. H. Koenderink, F. MacKintosh, and D. Bonn, *Physical Review Letters* **117**, 217802 (2016).
- [66] Y. Lin, N. Phan-Thien, and B. Cheong Khoo, *Journal of Rheology* **58**, 223 (2014).
- [67] B. Z. Dlugogorski, M. Grmela, and P. J. Carreau, *Journal of Non-Newtonian Fluid Mechanics* **48**, 303 (1993).
- [68] N. P. Thien and R. I. Tanner, *Journal of Non-Newtonian Fluid Mechanics* **2**, 353 (1977).
- [69] T. Schweizer, *Rheologica Acta* **41**, 337 (2002).
- [70] S. Granick and K. Binder, *Polymers in confined environments* (Springer, 2011).
- [71] J. Kirk, M. Kröger, and P. Ilg, *Macromolecules* **51**, 8996 (2018).
- [72] S. Cho, S. Jeong, J. M. Kim, and C. Baig, *Scientific Reports* **7**, 9004 (2017).
- [73] M. Tsige and S. S. Patnaik, *Chemical Physics Letters* **457**, 357 (2008).
- [74] S. Yasuda and R. Yamamoto, *Physical Review X* **4** (2014).
- [75] M. A. G. Cunha, P. D. Olmsted, and M. O. Robbins, *Journal of Rheology* **66**, 619 (2022).
- [76] A. Arnold, B. Bozorgui, D. Frenkel, B.-Y. Ha, and S. Jun, *The Journal of Chemical Physics* **127**, 164903 (2007).
- [77] T. C. O'Connor, N. J. Alvarez, and M. O. Robbins, *Physical Review Letters* **121**, 047801 (2018).
- [78] H.-Q. Xie and C.-H. Chang, *Communications Physics* **2**, 24 (2019).
- [79] S. Bernardi, B. D. Todd, and D. J. Searles, *The Journal of Chemical Physics* **132**, 244706 (2010).
- [80] D. T. Ta, A. K. Tieu, H. T. Zhu, and B. Kosasih, *The Journal of Chemical Physics* **143**, 164702 (2015).
- [81] C. Gattinoni, J. P. Ewen, and D. Dini, *The Journal of Physical Chemistry C* **122**, 20817 (2018).
- [82] K. Kanhaiya, S. Kim, W. Im, and H. Heinz, *npj Computational Materials* **7**, 17 (2021).
- [83] S. Napolitano, *Soft Matter* **16**, 5348 (2020).
- [84] J. Krim, *Advances in Physics* **61**, 155 (2012).
- [85] R. F. Apóstolo, G. Tsagaropoulou, and P. J. Camp, *Journal of Molecular Liquids* **277**, 606 (2019).

- [86] D. Savio, N. Fillot, P. Vergne, and M. Zaccheddu, *Tribology Letters* **46**, 11 (2012).
- [87] J.-M. Albina, A. Kubo, Y. Shiihara, and Y. Umeno, *Tribology Letters* **68**, 49 (2020).
- [88] S. L. Mayo, B. D. Olafson, and W. A. Goddard, *The Journal of Physical Chemistry* **94**, 8897 (1990).
- [89] S. K. Das, M. M. Sharma, and R. S. Schechter, *The Journal of Physical Chemistry* **100**, 7122 (1996).
- [90] C. McCabe, S. Cui, P. T. Cummings, P. A. Gordon, and R. B. Saeger, *The Journal of Chemical Physics* **114**, 1887 (2001).
- [91] J. Ewen, C. Gattinoni, F. Thakkar, N. Morgan, H. Spikes, and D. Dini, *Materials* **9**, 651 (2016).
- [92] J. Vlachopoulos and N. Polychronopoulos, Basic concepts in polymer melt rheology and their importance in processing, in *Applied Polymer Rheology*, pp. 1–27, John Wiley & Sons, Inc., 2011.
- [93] B. V. Raghavan and M. Ostoja-Starzewski, *Physics of Fluids* **29**, 023103 (2017).
- [94] M. Morciano, M. Fasano, A. Nold, C. Braga, P. Yatsyshin, D. N. Sibley, B. D. Goddard, E. Chiavazzo, P. Asinari, and S. Kalliadasis, *The Journal of Chemical Physics* **146**, 244507 (2017).
- [95] J. P. Ewen, C. Gattinoni, N. Morgan, H. A. Spikes, and D. Dini, *Langmuir* **32**, 4450 (2016).
- [96] J. N. Israelachvili, *Intermolecular and surface forces* (Academic Press is an imprint of Elsevier, 2012).

Supplemental Material: Molecular Rheology of Nanoconfined Polymer Melts

Ahmet Burak Yıldırım,¹ Aykut Erbaş,^{2,3} and Luca Biancofiore^{1,2}

¹*Department of Mechanical Engineering, Bilkent University, 06800 Ankara, Turkey*

²*UNAM - National Nanotechnology Research Center and Institute of Materials Science & Nanotechnology, Bilkent University, 06800 Ankara, Turkey*

³*Institute of Physics, University of Silesia, Katowice, Poland*

(Dated: March 17, 2023)

SIMULATION DETAILS

The work includes two types of simulations: (i) diffusion to determine the relaxation times and (ii) shear to determine the viscoelastic response. For both types, the interactions between all atoms are modelled by the standard 12/6 Lennard-Jones potential using DREIDING force field [1, 2], with the cutoff radius of $r_c = 9.85 \text{ \AA}$ and the time-integration is performed for the timestep of $\tau = 1 \text{ fs}$.

For (i), each simulation box contains $N = 216$ charge-neutral linear or star $\text{C}_{25}\text{H}_{52}$ polymers equilibrated at $T = 372 \text{ K}$ at a pressure at $p = 1 \text{ atm}$ [3]. The resultant melt density of $\rho = 0.63 \text{ g/cm}^3$ is expected as DREIDING potential is known to underestimate the density of the polymer melts while giving accurate viscosity estimations [4]. Preserving the density does not guarantee that hydrostatic pressures are also identical between the systems; the hydrostatic pressures are also prone to variations in the confinement level, chain topology, and rigidity. However, since we are mainly interested in acquiring identical geometric confinements and densities for all of our melt systems, we disregard the variations in hydrostatic pressure between the systems [5] but rather track the change in the flow-dependent (i.e., dynamic) components of the stress tensor. This helps us to construct $N_1, N_2, \sigma^{(\text{VE})}$ independently of the hydrostatic pressure to study the rheological response. We track the mean-square end-to-end vectors for $t = 10^8 \tau$ under NVE dynamics regulated at $T = 372 \text{ K}$ using the Langevin thermostat with a damping coefficient of 100τ . We later fit the correlation function following $\langle \mathbf{r}_{\text{ee}}(t) \cdot \mathbf{r}_{\text{ee}}(0) \rangle / \langle \mathbf{r}_{\text{ee}}(0) \cdot \mathbf{r}_{\text{ee}}(0) \rangle = A \exp(-t/\lambda)$, with constant $A (\approx 1$ for each fit).

For (ii), the simulation boxes contain varying N polymers, depending on the box size or confinement level, while keeping the density N/V constant for the volume V . For the bulk system, we run shear simulations by deforming the cubic simulation box ($h = 5.82 \text{ nm}$, resulting in $p = 1 \text{ atm}$ for unaltered star polymer) under constant volume and temperature by solving SLOD equations of motion [6] at $T = 372 \text{ K}$ with a damping coefficient of 100τ . For the confined melts, we run shear simulations under NVE dynamics at $T = 372 \text{ K}$ using the Langevin thermostat ($N = 216$ for box dimensions: $6.35 \text{ nm} \times 5.57 \text{ nm} \times 6.97 \text{ nm}$) with a damping coefficient of 10τ , which is achieved by moving the top and bottom surfaces at constant velocity in the x-direction [7]. While investigating the confinement effect on N_1 and N_2 , we changed the number of polymers N , accordingly (i.e., $N = 216, h = 5.57 \text{ nm}$). The thermostat is only applied to the non-sheared directions to preserve the increase in velocity due to shear correctly. The fixed and rigid wall configuration consists of five hematite ($\alpha - \text{Fe}_2\text{O}_3$) layers on the top and bottom surfaces [8], which results in a wall thickness of 1.31 nm to ensure a negligible wall deformation compared to thin and deformable walls. Unlike soft walls with variable film thickness, rigid walls are known to experience higher load variations, making them a better choice for observing the magnified confinement effects [9]. A Couette flow is simulated for $10^6 - 2 \times 10^7 \tau$, ensuring that a typical polymer chain passes through the periodic boundaries at least three times, eliminating the transient response. The damping coefficients are selected to ensure that the temperature remains $\sim 372 \pm 0.1 \text{ K}$ throughout the simulations.

Note that the volume of the bulk and confined systems differ due to wall interactions; hence $p = 1 \text{ atm}$ is preserved for unaltered star polymers while determining the volume of both linear and star polymer systems. This enables us to validate some of the results for star polymers with Ref. [3].

CRYSTALLIZATION

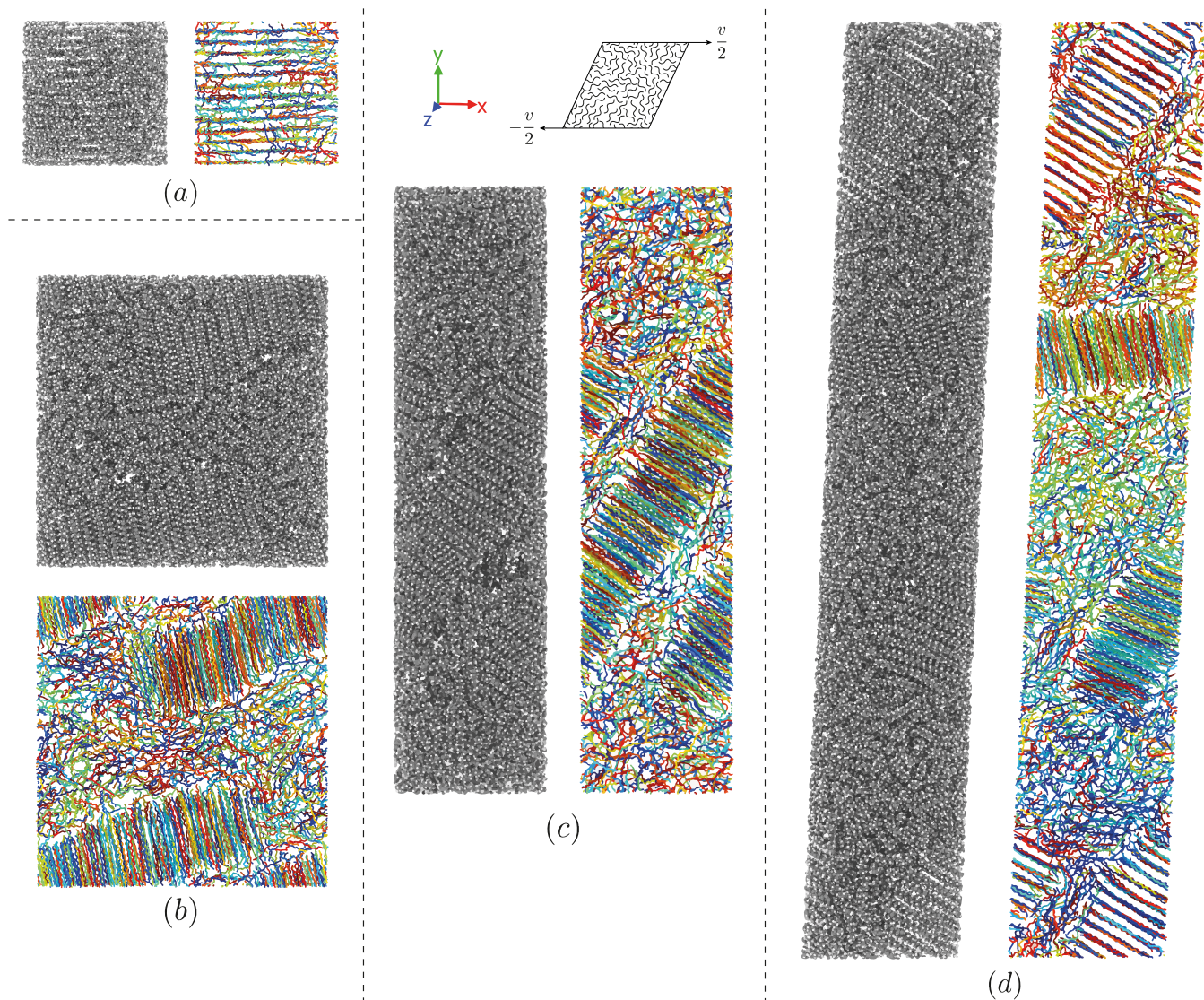


FIG. S1. Snapshots of the crystalline structure formation of unaltered linear polymer melt ($k_{\theta} = \epsilon$) under shear for different simulation box sizes. The shear rate is $\dot{\gamma} = 6 \times 10^8 s^{-1}$, corresponding to $Wi = 12.48$. Size of the simulation boxes for (a) is (h, h, h) , (b) is $(2h, 2h, h)$, for (c) is $(h, 4h, h)$, and (d) is $(h, 6h, h)$ where $h \approx 5.82 \text{ \AA}$ to retain the identical density of $\rho = 0.63 \text{ g/cm}^3$. Under identical settings, star polymer melts do not exhibit crystallization. For each simulation box size, molecular and bond configurations are illustrated separately, where the coloring of the bonds is random.

SLIP

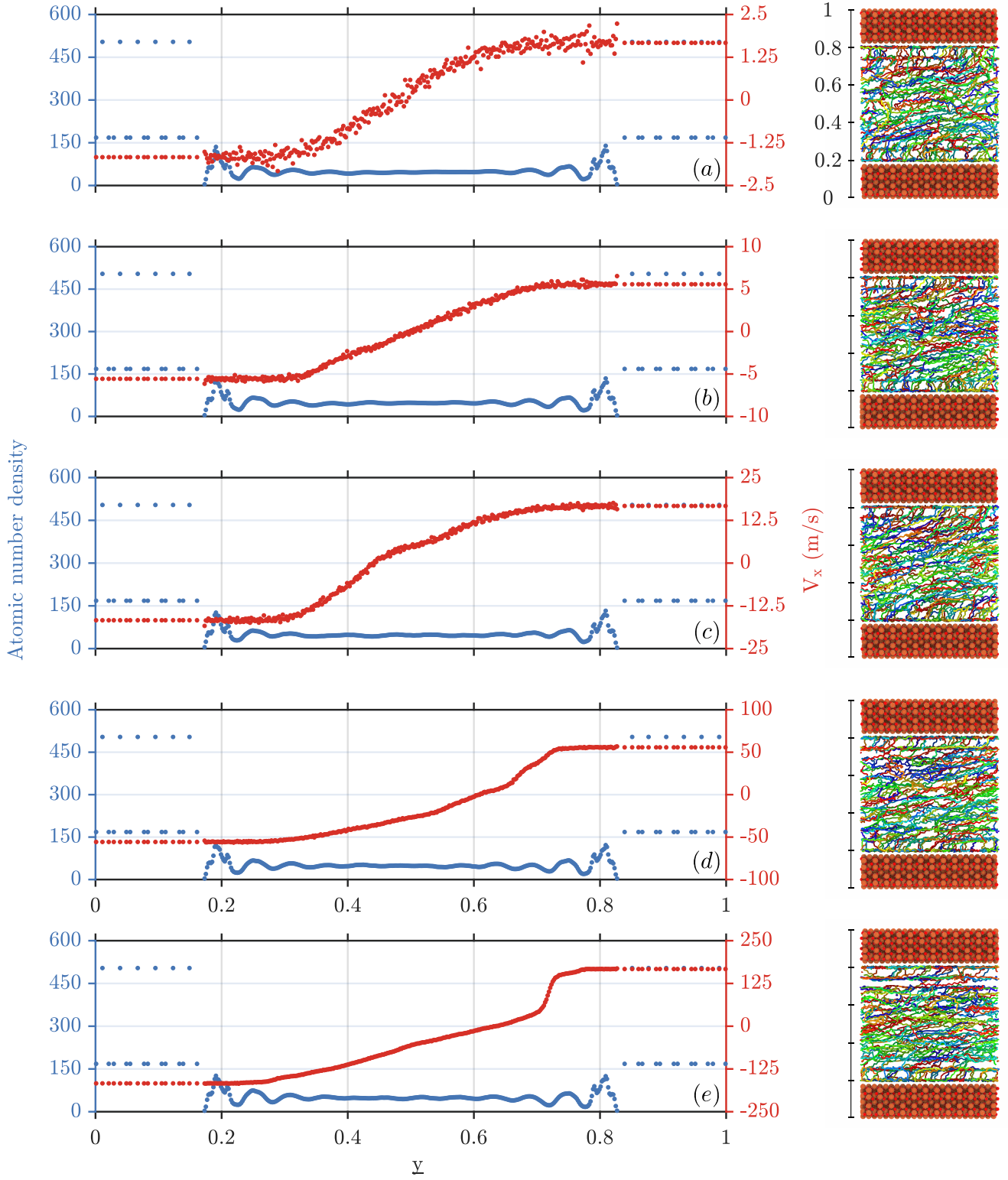


FIG. S2. The steady-state spatial configuration and the velocity distribution of the atoms within the shear of confined linear polymer melts for $h = 5.57\text{\AA}$. The shear rate is (a) $\dot{\gamma} = 6 \times 10^8 s^{-1}$, (b) $\dot{\gamma} = 6 \times 10^9 s^{-1}$, (c) $\dot{\gamma} = 6 \times 10^{10} s^{-1}$, (d) $\dot{\gamma} = 6 \times 10^{11} s^{-1}$, and (e) $\dot{\gamma} = 6 \times 10^{12} s^{-1}$, as a function of the normalized vertical component y . The corresponding Weissenberg numbers are (a) $Wi = 12.48$, (b) $Wi = 124.8$, (c) $Wi = 1248$, (d) $Wi = 12480$ and (e) $Wi = 124800$. The snapshots of the simulation box given on the left illustrate the carbon-carbon bond configuration of the system, where the coloring of the bonds is random.

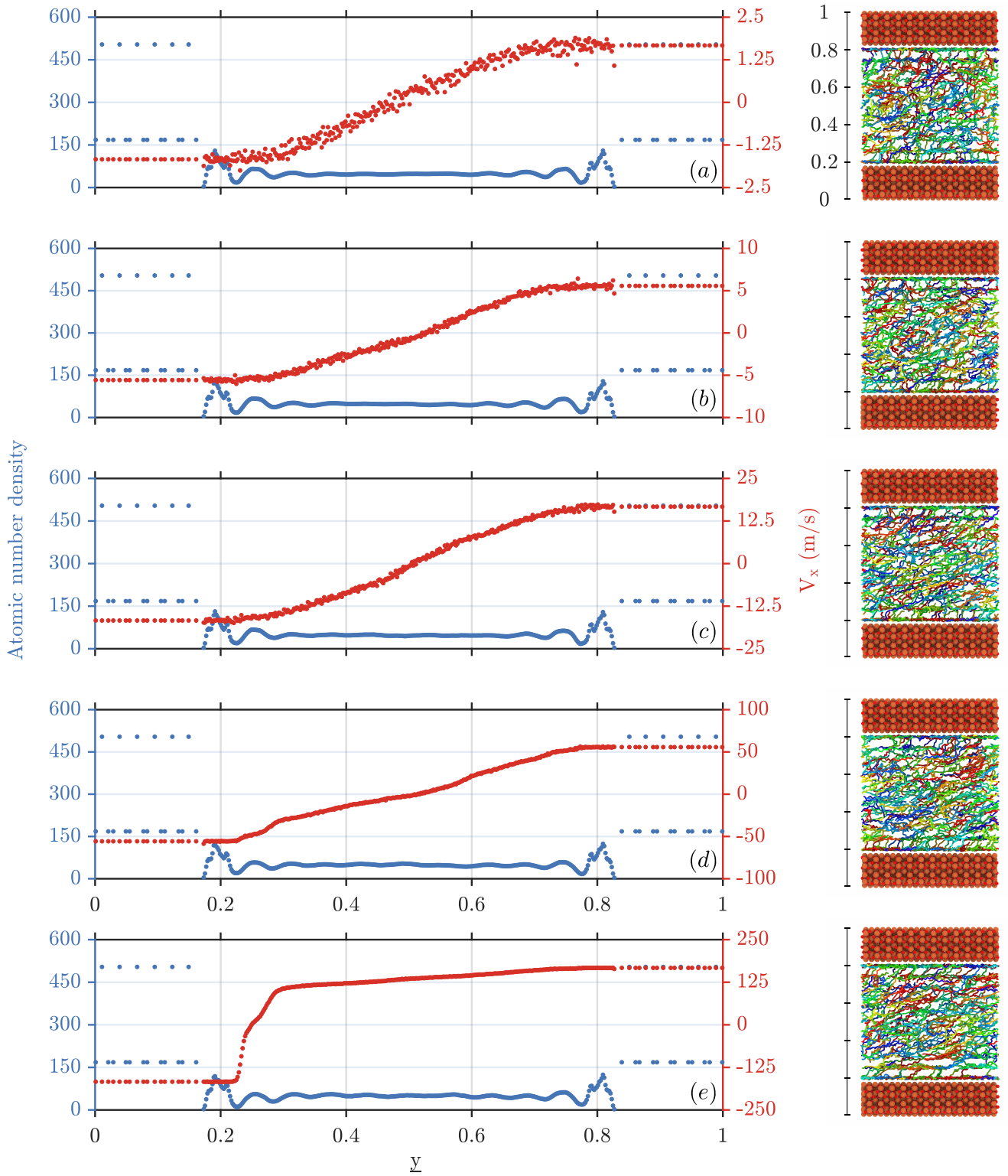


FIG. S3. The steady-state spatial configuration and the velocity distribution within the shear of confined star polymer melts where $h = 5.57\text{\AA}$. The shear rate is (a) $\dot{\gamma} = 6 \times 10^8 \text{s}^{-1}$, (b) $\dot{\gamma} = 6 \times 10^9 \text{s}^{-1}$, (c) $\dot{\gamma} = 6 \times 10^{10} \text{s}^{-1}$, (d) $\dot{\gamma} = 6 \times 10^{11} \text{s}^{-1}$, and (e) $\dot{\gamma} = 6 \times 10^{12} \text{s}^{-1}$, as a function of the normalized vertical component y . The corresponding Weissenberg numbers are (a) $Wi = 5.46$, (b) $Wi = 54.6$, (c) $Wi = 546$, (d) $Wi = 5460$, and (e) $Wi = 54600$. The snapshots of the simulation box given on the left illustrate the carbon-carbon bond configuration of the system, where the coloring of the bonds is random.

MONOMERS

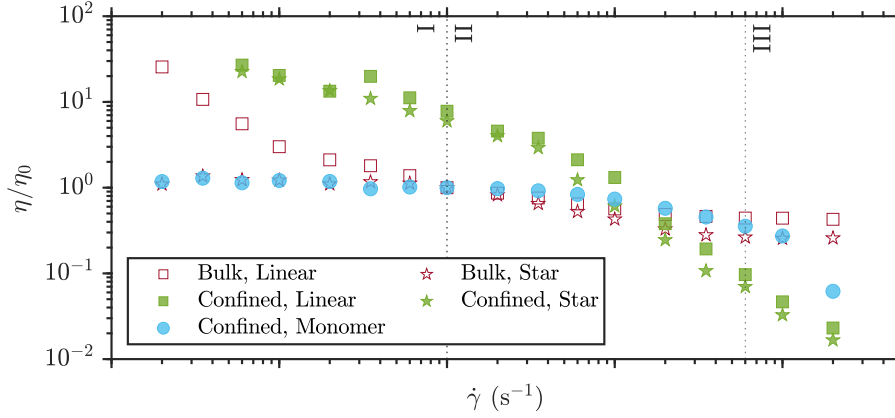


FIG. S4. The normalized viscosity of monomers under confinement, obtained by breaking all the carbon-carbon bonds of the linear polymer melt, together with linear and star polymer melts in bulk and under confinement. Linear and star polymers have the unaltered configuration ($k_\theta = \epsilon$), whereas k_θ does not apply for the monomers. I, II, and III indicate the 1st Newtonian plateau, the shear-thinning regime, and the 2nd Newtonian plateau for bulk polymers, respectively.

RADIUS OF GYRATION

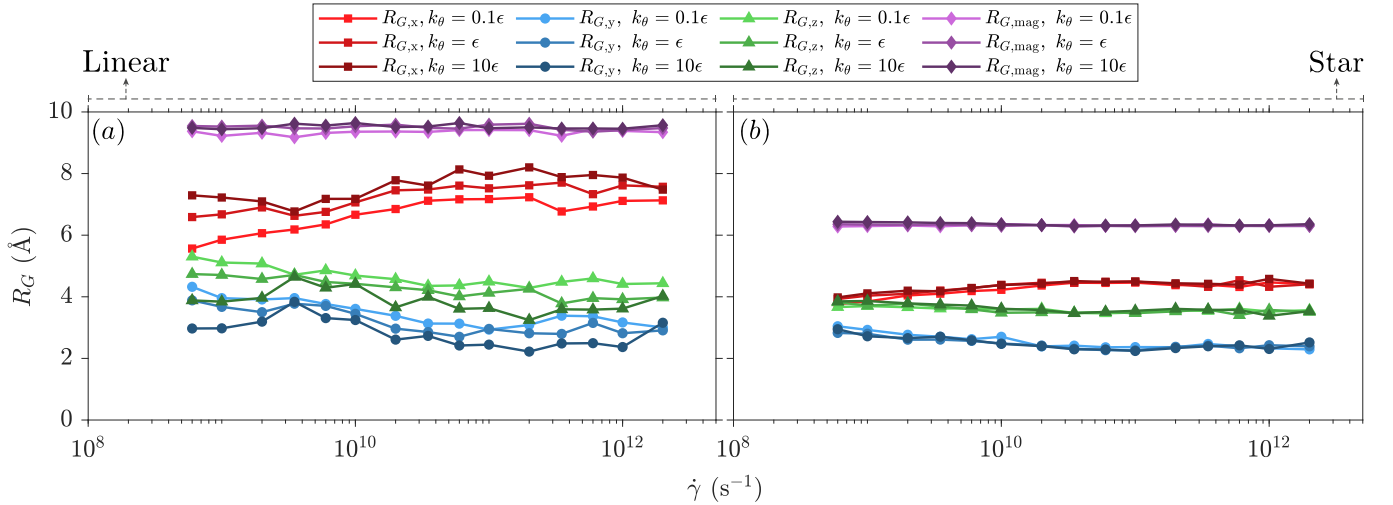


FIG. S5. Steady-state radii of gyration (R_G) for confined linear and star polymer melts where $h = 5.57\text{\AA}$. The x , y , and z components of the radius of gyration, together with the overall magnitude, are given for linear (a) and star (b) polymers. The overall magnitudes $R_{G,\text{mag}}$ do not show significant dependency with $\dot{\gamma}$, the average values read $R_{G,\text{linear}}^{(0.1\epsilon)} = 9.34\text{\AA}$, $R_{G,\text{linear}}^{(\epsilon)} = 9.50\text{\AA}$, $R_{G,\text{linear}}^{(10\epsilon)} = 9.52\text{\AA}$; $R_{G,\text{star}}^{(0.1\epsilon)} = 6.32\text{\AA}$, $R_{G,\text{star}}^{(\epsilon)} = 6.31\text{\AA}$, and $R_{G,\text{star}}^{(10\epsilon)} = 6.36\text{\AA}$.

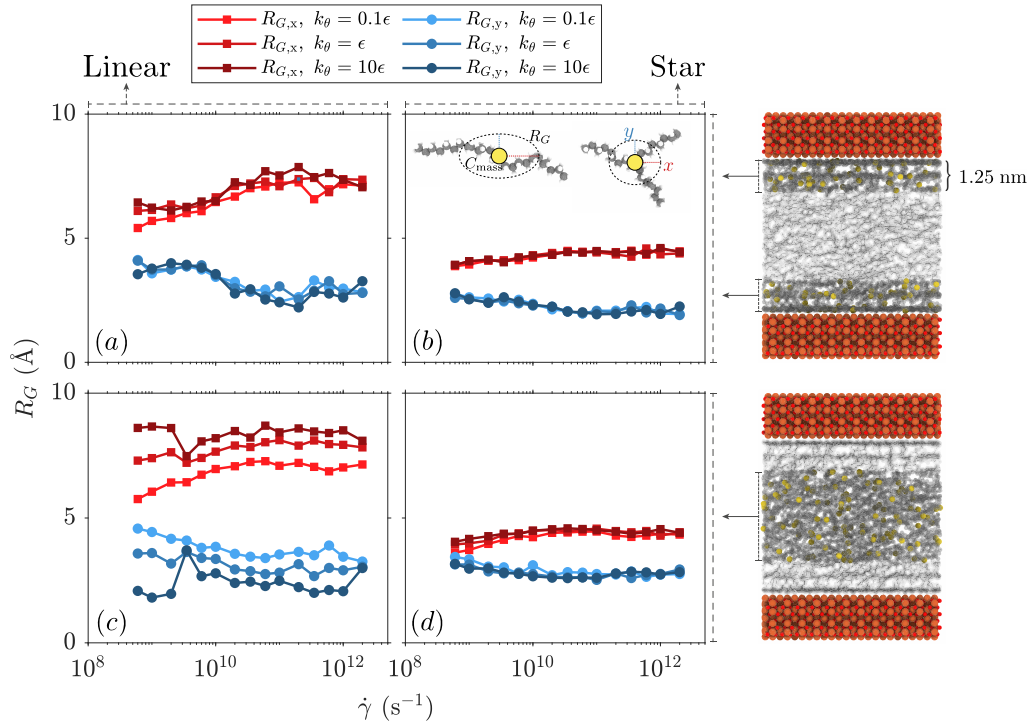


FIG. S6. Near/away from the surface steady-state radii of gyration (R_G) for confined linear and star polymer melts where $h = 5.57\text{\AA}$. The x and y components of the radius of gyration are given near the surface for linear (a) and star (b) polymers; away from the surface for linear (c) and star (d) polymers. Especially for star polymers, the relation between viscoelastic load and near-surface dynamics cannot be captured using radii of gyration. The snapshots depict the regions where the components of the radii of gyrations are calculated based on the positions of the center of mass of each chain, whose approximate positions are shown in yellow for a single timestep.

-
- [1] S. L. Mayo, B. D. Olafson, and W. A. Goddard, *The Journal of Physical Chemistry* **94**, 8897 (1990).
 - [2] S. K. Das, M. M. Sharma, and R. S. Schechter, *The Journal of Physical Chemistry* **100**, 7122 (1996).
 - [3] C. McCabe, S. Cui, P. T. Cummings, P. A. Gordon, and R. B. Saeger, *The Journal of Chemical Physics* **114**, 1887 (2001).
 - [4] J. Ewen, C. Gattinoni, F. Thakkar, N. Morgan, H. Spikes, and D. Dini, *Materials* **9**, 651 (2016).
 - [5] J. Vlachopoulos and N. Polychronopoulos, Basic concepts in polymer melt rheology and their importance in processing, in *Applied Polymer Rheology*, pp. 1–27, John Wiley & Sons, Inc., 2011.
 - [6] B. V. Raghavan and M. Ostoja-Starzewski, *Physics of Fluids* **29**, 023103 (2017).
 - [7] M. Morciano, M. Fasano, A. Nold, C. Braga, P. Yatsyshin, D. N. Sibley, B. D. Goddard, E. Chiavazzo, P. Asinari, and S. Kalliadasis, *The Journal of Chemical Physics* **146**, 244507 (2017).
 - [8] J. P. Ewen, C. Gattinoni, N. Morgan, H. A. Spikes, and D. Dini, *Langmuir* **32**, 4450 (2016).
 - [9] J. N. Israelachvili, *Intermolecular and surface forces* (Academic Press is an imprint of Elsevier, 2012).